PCCP

PAPER

View Article Online
View Journal | View Issue

Check for updates

Cite this: *Phys. Chem. Chem. Phys.*, 2022, **24**, 22437

Fragmentation of interstellar methanol by collisions with He$^{\bullet+}$: an experimental and computational study†

Vincent Richardson,[a] Emília Valença Ferreira de Aragão,[bc] Xiao He,[a] Fernando Pirani,[bd] Luca Mancini,[b] Noelia Faginas-Lago,[bc] Marzio Rosi,[d] Luca Matteo Martini[a] and Daniela Ascenzi*[a]

Methanol is a key species in astrochemistry as its presence and reactivity provides a primary route to the synthesis of more complex interstellar organic molecules (iCOMs) that may eventually be incorporated in newly formed planetary systems. In the interstellar medium, methanol is formed by hydrogenation of CO ices on grains, and its fate upon collisions with interstellar ions should be accounted for to correctly model iCOM abundances in objects at various stages of stellar evolution. The absolute cross sections (CSs) and branching ratios (BRs) for the collisions of He$^{\bullet+}$ ions with CH_3OH are measured, as a function of the collision energy, using a Guided Ion Beam Mass Spectrometer (GIB-MS). Insights into the dissociative electron (charge) exchange mechanism have been obtained by computing the entrance and exit multidimensional Potential Energy Surfaces (PESs) and by modelling the non-adiabatic transitions using an improved Landau–Zener–Stückelberg approach. Notably, the dynamical treatment reproducing the experimental findings includes a strong orientation effect of the system formed by the small He$^{\bullet+}$ ion and the highly polar CH_3OH molecule, in the electric field gradient associated to the strongly anisotropic intermolecular interaction. This is a stereodynamical effect that plays a fundamental role in collision events occurring under a variety of conditions, with kinetic energy confined within intervals ranging from the sub-thermal to the hyper-thermal regime.

Received 30th May 2022,
Accepted 6th September 2022

DOI: 10.1039/d2cp02458f

rsc.li/pccp

1 Introduction

Methanol (CH_3OH) is one of the most abundant and ubiquitous interstellar Complex Organic Molecules (iCOMs)[1] with countless detections in various environments, from molecular clouds to comets. Methanol is a key astrochemical molecule because its reactivity represents a major route to the synthesis of more complex organic species such as esters, ketones and aldehydes, that are the prebiotic precursors of sugars, amino acids and other biomolecules.[2–4]

Since its first interstellar detection in 1970,[5] methanol has been regularly detected at various stages of stellar evolution, from the cold and dark pre-stellar core phase (see ref. 6 and refs therein) to the protostar phase, where it has been widely observed towards hot cores and hot corinos, the gas phase envelopes surrounding young stellar objects of high or low masses, under either warm or cold conditions (see for instance[7–11] for the most recent surveys of iCOMs detections in Class 0 and Class I Solar-like protostars). At the protostellar stage, methanol is also detected in shocked gases associated with low-mass protostellar outflows.[12] Although with more difficulty, CH_3OH has been detected in protoplanetary disks, the next stage of stellar evolution which directly precedes the formation of a planetary system, thereby demonstrating that methanol, and consequently larger iCOMs, are present at the planet formation stage.[13–17] CH_3OH has been detected as a volatile species in several comets, including 67P/Churyumov-Gerasimenko by the recently concluded Rosetta mission,[18–20] as ice on the surface of a Kuiper Belt Object (KBO)[21] and it is among the few iCOMs detected in other galaxies.[22]

Chemical modelling, experimental determinations and astronomical observations[23–25] have clearly established that methanol observed in regions of star formation is synthesized by successive hydrogenation of CO-rich ice mantles.[3,4] Following formation, it can be released into the gas phase *via* thermal

---

[a] *Department of Physics, University of Trento, Trento, Italy. E-mail: daniela.ascenzi@unitn.it*

[b] *Department of Chemistry, Biology and Biotechnology, Università degli studi di Perugia, Perugia, Italy*

[c] *Master-Tec s.r.l., Via Sicilia 41, Perugia, Italy*

[d] *Department of Civil and Environmental Engineering, Università degli studi di Perugia, Perugia, Italy*

† Electronic supplementary information (ESI) available. See DOI: **https://doi.org/10.1039/d2cp02458f**

desorption under warm conditions or *via* non-thermal desorption processes (*i.e.* by gaining desorption energy *via* interactions with photons, electrons, cosmic rays, grain–grain collisions or exothermic chemical reactions in the solid phase) in cold environments. Once in the gas phase, methanol can contribute to synthesize more complex species *via* neutral–neutral or ion–neutral reactions. For instance, it can be protonated by reactions with H_3^+ or HCO^+ ions and further react with either CH_3OH or HCOOH to eventually lead to the formation of dimethyl ether and methylformate, respectively.[26,27] Additionally, H abstraction by the hydroxyl (OH) radical can lead to formation of H_2O plus CH_2OH/CH_3O.[28]

To explain the abundance of methanol, that in some astronomical environments can be as high as 3×10^{-5} with respect to H_2,[1] accurate measurements of the rate constants for formation and destruction routes are required. In addition to interactions with photons and electrons, reactions with ions are among the main destruction routes for methanol. The most relevant ions in this respect are H^+, $He^{\bullet+}$ and H_2^+, which are formed by the interaction of cosmic rays with H or He, as well as H_2. From H^+ and H_2^+, H_3^+ and HCO^+ can be produced by ion-molecule reactions with H_2 and CO, two of the most abundant neutrals in the ISM. Reactions with $He^{\bullet+}$, H_3^+ and HCO^+ are therefore expected to be the dominant destruction mechanisms for the vast majority of iCOMs, including methanol. However, while H_3^+ and HCO^+ reactions involve proton transfer processes which can be, but are not necessarily, dissociative, the large recombination energy of $He^{\bullet+}$, is expected to lead to a greater degree of methanol dissociation.

While the reactions of H_3^+ [29,30] and HCO^+ [30–32] with CH_3OH have been amply studied, to the best of our knowledge, no previous experimental or theoretical studies have been performed on the reaction of $He^{\bullet+}$ and the rate constant and branching ratios (BRs) reported in the astrochemical databases KIDA (KInetic Database for Astrochemistry[33] available at **https://kida.astrochem-tools.org/**) and UDfA (UMIST Database for Astrochemistry[34] available at **https://udfa.ajmarkwick.net/**) are estimates based on chemical analogies and simple modelling of ion–neutral reactivity. Though such estimates can be useful when experimental/computational values are not available, they can sometimes differ significantly from the true values, as demonstrated by previous work on the reactivity of $He^{\bullet+}$ with dimethyl ether (CH_3OCH_3) and methyl formate ($HCOOCH_3$),[35–37] for which the rate coefficients, BRs and their temperature dependences have been found to differ substantially from the estimates reported in the databases, as a consequence of stereodynamical effects present at low collision energies.

In this paper we report the first experimental determination of the partial and total ionization cross sections (CSs) of CH_3OH upon collisions with $He^{\bullet+}$ ions as a function of the collision energy (in the range from $\sim$0.04 to $\sim$10 eV) using guided ion beam mass spectrometry. Experimental results are interpreted by an improved Landau–Zener approach based on an analytical expression of the Potential Energy (hyper)Surfaces (PESs) for the entrance and exit channels leading to the formation of the $CH_3OH^{\bullet+}$ radical cation in highly excited electronic states. The PESs have been obtained by a semi-empirical method, where involved parameters, defined on phenomenological ground, have a proper physical meaning, thus guaranteeing an internally consistent representation of the interaction in the full space of the relative configuration of reagents. This is a key prerequisite to carry out molecular dynamics simulations over a range of collision energies that extends from sub-thermal up to hyper-thermal values. Moreover, the internal energy content of the resultant molecular ion is such that several fragmentation channels are energetically accessible.

In the entrance channel a natural orientation of a polar reagent, such as CH_3OH, occurs because of the large electric field gradients probed by the rotating molecule within the strongly anisotropic PES, arising from the intermolecular interaction with the very small $He^{\bullet+}$ cation. This polarization effect leads to the preferential formation of the non covalent adduct (the precursor state of reaction) in specific configurations confined within a narrow angular cone, giving rise to the so called pendular states.[38,39] In other words, the most stable configurations of the precursors are rather different with respect to the transition state promoting direct electron transfer, and this generates a pronounced steric effect on the dynamical evolution of reactive events. Such stereodynamical effects become increasingly significant at low collision energies.

Comparison of the experimental results with the model outcomes indicates that the preferential geometries assumed by the reagents at low collision energies inhibit charge exchange, thus giving rate coefficients at low temperatures (most relevant for the interstellar medium) that differ substantially from those reported in astrochemical databases. Note that, for the title reaction, the routinely used capture theory methods overestimate the experimental absolute cross section values and are unable to reproduce their energy dependence in the probed energy range, providing divergent results at low collision energies (see also ref. 35–37). *Ab initio* calculations are used to define the shape of the molecular orbitals of the methanol molecule from which the electron is captured and to evaluate the energetics of the various fragmentation channels of the $CH_3OH^{\bullet+}$ radical cation.

2 Experimental

2.1 Experimental methodology

The experimental data presented as part of this work have been collected using the Trento Guided Ion Beam Mass Spectrometer (GIB-MS), which has been described in detail previously[40,41] and so it is only covered briefly here. The Trento GIB-MS is a tandem mass spectrometer composed of two octopoles (O) and two quadrupole mass filters (Q) in a O–Q–O–Q configuration that allows for the investigation of bimolecular reactions of mass-selected ions. Absolute CSs and BRs as a function of the collision energy (E_{CM}) are derived by measuring the yields of both parent and product ions.

$He^{\bullet+}$ ions are produced by electron ionization at electron energies in the range 55–65 eV. Electrons are emitted by a thoriated tungsten filament with the emission current stabilized by an electronic feedback mechanism. He is introduced into the ion source by a variable leak valve (Agilent Technologies/Varian model 951-5106) at pressures in the range 10^{-7}–10^{-8} mbar.

Following ionization, ions pass through the first octopole, which acts as a ion guide, before being mass selected by the first quadrupole. Reactions occur in the second octopole, which is surrounded by a 10 cm long scattering cell. The pressure of the neutral gas in the scattering cell surrounding the second octopole is monitored by a spinning rotor gauge (SRG2 MKS Instruments, MA, USA). In order to be able to convert experimental CSs to absolute CSs, calibration experiments have been performed on the $He^{\bullet+} + SiCl_4$ system, which is the subject of previous study using a similar set-up,[42] details of which are given in the ESI.† In this way, an effective cell length value equal to 8.3 ± 4.0 cm has been obtained, with the magnitude of the uncertainty resulting from the literature CSs used in the calibration.[42]

The collision energy in the laboratory frame is dependent on both the reagent ion charge (+1 in the case of this work) and the difference between the ion source and reaction cell potentials. The retarding potential method was applied to the reagent ion beam[43] to determine the maximum of the first derivative of the reagent ion yield, which defines the zero of the kinetic energy. In this way, we have estimated an average reagent ion beam FWHM of $\sim$1 eV in the laboratory frame, equivalent to $\sim$0.9 eV in the center-of-mass (CM) frame. By varying the potentials of the second octopole and all subsequent optics, we are able to scan a collision energy range from $\sim$0.05 to $\sim$10 eV in the CM frame (E_{CM}).

The reaction cell is filled with a $\sim$10% mixture of CH_3OH in Ar at variable pressures in the range of 1.0×10^{-8} to 1.3×10^{-4} mbar. The dilution of CH_3OH in Ar is performed in order both to stabilise the vapour pressure of CH_3OH and to keep any secondary reaction at a reduced level. The chosen pressure interval further aids to limit the impact of secondary reactions, while still providing an accurate pressure measurement and a dynamic range from 10^{-1} to 10^{2} Å^2 for the absolute CSs.

In order to limit the effects of potential drifts in source pressure, reaction cell pressure and electron emission current, data are collected in the so-called multi-scan mode, where signals are recorded for parent ($He^{\bullet+}$) and product ions at a single point (*e.g.* at a specific E_{CM} or CH_3OH pressure in the collision cell) before moving to the next one. To account for potential differences in the collection efficiency of $He^{\bullet+}$ ions when the collection optics are optimized for product ions, parent ion intensities have been recorded at the product ion optimisation with gas (CH_3OH/Ar mixture in the present case) in the scattering cell ($I_{Prod}(CM)$). Subsequently, the $I_{Prod}(CM)$ is re-scaled to give the real $He^{\bullet+}$ intensity ($I_{Par}(CM)$) by optimizing the collection optics at the parent ion with no gas in the cell and using eqn (1):

$$I_{Par}(CM) = I_{Prod}(CM) \cdot \frac{I^{Ref}_{Par}}{I^{Ref}_{Prod}} \qquad (1)$$

where I^{Ref}_{Par} and I^{Ref}_{Prod} are the intensities of the parent ion, without gas in the reaction cell, at a reference E_{CM} when the collection optics are optimized for the parent and product ions, respectively.

2.2 Experimental results

By recording mass spectra at different neutral gas pressures charged products from the reaction of $He^{\bullet+}$ with CH_3OH have been identified at *m*/*z* 14, 15, 28, 29 and 31. Additional peaks observed at *m*/*z* 33, 41 and 47 have been identified as deriving from secondary reaction of the *m*/*z* 29 product with both Ar and CH_3OH (see the ESI† for a typical mass spectrum). Notably, as we do not observe a product at *m*/*z* 32, corresponding to the formation of $CH_3OH^{\bullet+}$, we are able to conclude that the electron transfer process is completely dissociative.

The limited resolution of our quadrupole mass spectrometer at *m*/*z* = 1 and 2 makes it infeasible to obtain results at these masses. Hence, potential products at such *m*/*z* values are not considered in the analysis. On the basis of previous results on the dissociative ionization of methanol *via* electrons and photons,[44,45] we can expect that the contribution of the neglected ions to total yield should not exceed a few percent. In particular, in the case of photons,[45] the BR for H^+ is 1% at 24.5 eV photon energy and 3% at 30 eV, with even smaller values for H_2^+ (0% and 0.3% at 24.5 and 30 eV photon energy respectively). Additionally, the AE of H_2^+ is measured to be 26.5 eV, which is higher than the recombination energy carried by $He^{\bullet+}$. Similarly, in the case of electrons[44] the BR for H^+ is 1.2% at 30 eV electron energy and 5.5% at 65 eV, with smaller values for H_2^+ (0.07% and 0.3% at 30 and 65 eV electron energy respectively). Therefore, in our case, an upper limit for BR(H^+) of $\sim$0.05 (a value that is within the experimental uncertainty for some products) can be assumed, while the formation of H_2^+ can be neglected.

The corresponding reaction pathways for the products are given in eqn (2)–(6) with the thermochemistries shown in Table 1, while the secondary reactions are described by eqn (7)–(9).

$$He^{\bullet+} + CH_3OH \rightarrow CH_2^{\bullet+} + H_2O/(OH^{\bullet} + H^{\bullet}) + He \qquad (2)$$

$$\rightarrow CH_3^{+} + OH^{\bullet} + He \qquad (3)$$

$$\rightarrow CO^{\bullet+} + 2H_2/(H_2 + 2H^{\bullet})/4H^{\bullet} + He \qquad (4)$$

$$\rightarrow HCO^{+}/HOC^{+} + H^{\bullet} + H_2 + He \qquad (5)$$

$$\rightarrow CH_2OH^{+}/CH_3O^{+} + H^{\bullet} + He \qquad (6)$$

$$HCO^{+} + Ar \rightarrow ArH^{+} + CO \qquad (7)$$

$$HCO^{+} + CH_3OH \rightarrow CH_3OH_2^{+} + CO \qquad (8)$$

$$CH_3OH_2^{+} + CH_3OH \rightarrow (CH_3)_2OH^{+} + H_2O \qquad (9)$$

Reaction (8) has been studied extensively in literature, and its rate constant is reported to be in the range of 1.4×10^{-9} [30,32] to 2.7×10^{-9} cm^3 s^{-1},[30,46] while rate constants for reaction (9)

Table 1 Reaction thermochemistries (Δ*H*) for the identified products of the reaction of $He^{\bullet +}$ with methanol (CH_3OH) using literature data[a] and our calculations[b]

Reaction products	Eqn	Reaction enthalpy[a] (eV)	Reaction enthalpy[b] (eV)
$CH_2^{\bullet +} + H_2O + He$	(2a)	-10.56 ± 0.10^c	−10.66
$CH_2^{\bullet +} + OH^\bullet + H^\bullet + He$	(2b)	-5.41 ± 0.10^c	−5.60
$CH_3^+ + OH^\bullet + He$	(3)	-10.77 ± 0.10^d	−10.86
$CO^{\bullet +} + 2H_2 + He$	(4a)	-9.64 ± 0.10^e	−9.61
$CO^{\bullet +} + H_2 + 2H^\bullet + He$	(4b)	-5.12 ± 0.10^e	−5.14
$CO^{\bullet +} + 4H^\bullet + He$	(4c)	-0.60 ± 0.10^e	−0.67
$HCO^+ + H^\bullet + H_2 + He$	(5a)	-11.67 ± 0.10^f	−11.66
$HOC^+ + H^\bullet + H_2 + He$	(5b)	-10.01 ± 0.10^f	−10.03
$CH_2OH^+ + H^\bullet + He$	(6a)	-12.89 ± 0.10^g	−12.89
$CH_3O^+ + H^\bullet + He$	(6b)	-9.31 ± 0.10^g	−9.41

[a] Calculated using formation enthalpies $\Delta_f H^\circ$ (298 K) of CH_3OH and of $He^{\bullet +}$ taken from Active Thermochemical Database[49] and NIST[48] respectively. Formation enthalpies $\Delta_f H^\circ$ (298 K) for the reaction products as indicated in notes *c–g*. [b] This work, at 298 K. [c] $\Delta_f H^\circ$ (298 K) of $CH_2^{\bullet +}$ from ref. 49, of H_2O and $H^\bullet$ from ref. 48 and of $OH^\bullet$ from ref. 51. [d] $\Delta_f H^\circ$ (298 K) of CH_3^+ from ref. 49. [e] $\Delta_f H^\circ$ (298 K) and IE of CO from ref. 48. [f] $\Delta_f H^\circ$ (298 K) of HCO^+ and HOC^+ from ref. 49. [g] $\Delta_f H^\circ$ (298 K) of CH_2OH^+ and CH_3O^+ from ref. 49.

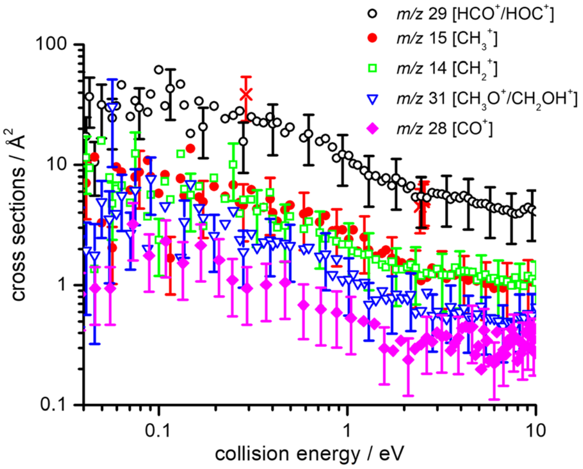

Fig. 1 Absolute CSs (in Å^2) for the production of HCO^+/HOC^+ (black open circles), CH_3^+ (red filled circles), CH_2^+ (green open squares), CH_3O^+/CH_2OH^+ (blue open triangles) and CO^+ (magenta filled diamonds) ionic products as a function of the collision energy (E_{CM}), from the title reaction.

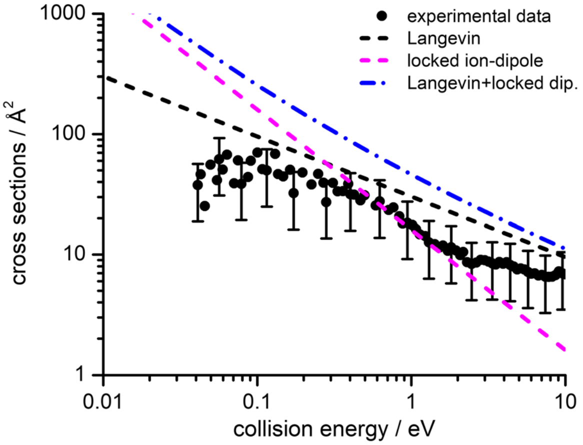

Fig. 2 Experimental total CSs for the electron exchange reaction of $He^{\bullet +}$ with CH_3OH as a function of the collision energy (E_{CM}). The black filled circles represent the measured total CSs, with error bars representing a 50% uncertainty on the absolute values of the cross-section. The lines represent total CSs as estimated from the following simple capture models: Langevin (black dashed line), locked-dipole (magenta dashed line) and the sum of the latter two models (blue dashed-dotted line). For the sake of clarity some of the error bars in the data points have been omitted, but for all data points the uncertainty on the absolute cross section value is approximately ±50% arising from the error propagation on the calibration of the effective cell length (see details in the ESI†).

have been reported in the range of 3×10^{-11} [30,32] to 4.6×10^{-10} cm^3 s^{-1}.[30,47] As the proton transfer from HCO^+/HOC^+ to Ar is endothermic by ∼2.3 and ∼0.65 eV respectively,[48,49] and no reaction was observed in previous studies of the process,[50] the observation of a minor *m*/*z* 41 product also indicates that a small proportion of the $[HCO]^+$ product ions are internally excited. We are therefore able to correct for the secondary reactions by summing the *m*/*z* 41, 33 and 47 products to the *m*/*z* 29 one, with the BRs calculated following this correction being given in Table 2, along with those currently available in literature.

Absolute CSs for the various channels have been recorded as a function of E_{CM} and results are shown in Fig. 1, where the data for *m*/*z* 29 $[HCO^+/HOC^+]$ include the correction for the contribution from secondary reaction products. For all products, we observe a decrease in CS with increasing E_{CM}, with no significant difference in trend being observed between the different channels. The total CSs (obtained by summing over all the channels) as a function of E_{CM} are reported in Fig. 2.

As our experimental set-up can only discriminate between product channels of different mass-to-charge (*m*/*z*) ratios, it is not possible to differentiate between different isomers of the ionic products (namely HCO^+/HOC^+ and CH_3O^+/CH_2OH^+) and between different combinations of the neutral co-products. Hence in Tables 1 and 2 all the thermochemically accessible combinations of products have been indicated.

Table 2 Product BRs for the reaction of $He^{\bullet +}$ with methanol (CH_3OH), both experimentally (with $P_{CH_3OH} = 1 \times 10^{-5}$ mbar and E_{CM} = 0.29 eV) and from literature

Reaction products	Eqn	BR[a]	BR[b]	BR[c]
$CH_2^{\bullet +} + H_2O/(OH^\bullet + H^\bullet) + He$	(2a and b)	0.08 ± 0.02	—	—
$CH_3^+ + OH^\bullet + He$	(3)	0.10 ± 0.03	0.50	0.50
$OH^+ + CH_3^\bullet + He$	—	—	0.50	0.50
$CO^{\bullet +} + 2H_2/(H_2 + 2H^\bullet)/(4H^\bullet) + He$	(4a–c)	0.03 ± 0.02	—	—
$HCO^+/HOC^+ + H^\bullet + H_2 + He$	(5a and b)	0.74 ± 0.18	—	—
$CH_2OH^+/CH_3O^+ + H^\bullet + He$	(6a and b)	0.05 ± 0.04	—	—

[a] This work. [b] From KIDA database.[33,52] [c] From UDfA (UMIST Database for Astrochemistry).[34,53]

It is interesting to compare the experimental BRs observed here, upon dissociative ionization of methanol by collisions with $He^{\bullet +}$, with other experimental investigations using electrons or photons as the ionizing agents. Regarding electron ionization, numerous measurements have been reported on relative partial ionization CSs of methanol for ionizing electron energies from 20 to 500 eV (see ref. 44, 54–57 and references therein). In all cases and at all ionizing electron energies, the primary product is CH_3O^+/CH_2OH^+ (with a BR equal to 0.37 at an electron energy of 30 eV that decreases to 0.30 at 100 eV, according to ref. 44). Conversely, the HCO^+/HOC^+ fragment, that is the major product in this work, has a BR of 0.18 that only marginally increases (to 0.20) at 100 eV.

The photodissociation of methanol upon single photon absorption in the gas phase has been amply studied both experimentally[45,58–62] and theoretically.[63] Relative or absolute photoionization CSs for the production of both the molecular and fragment ions have been measured in the VUV region, from the ionization threshold[58,59] up to 80 eV,[45] as well as in the X ray region,[64] using Photoelectron Photoion Coincidence (PEPICO) spectroscopy[60,61,64] and dipole (*e*, *e* + *ion*) spectroscopy.[45] The most relevant study to compare with present results is from Burton *et al.*,[45] where photoionization efficiencies and ionic photofragmentation BRs have been measured/calculated up to 80 eV. The explored energy range includes photoionization from the inner valence orbitals of CH_3OH that are involved in the charge exchange with $He^{\bullet+}$, as detailed in Section 3. Experimental values at a photon energy of 24.5 eV (close to the ionization energy of He) give CH_3O^+/CH_2OH^+ as the most abundant fragment (BR = 0.306), followed by the HCO^+/HOC^+ fragment (BR = 0.244). When the photon energy is increased to 80 eV the amount of CH_3O^+/CH_2OH^+ fragment decreases (BR = 0.169) and the HCO^+/HOC^+ ion becomes the dominant one (BR = 0.215). This is in line with the results from a PEPICO study on the dissociative photoionization of energy selected methanol radical cations (with an internal energy up to ∼7 eV)[61] where, at the highest internal energy of ∼7 eV, the fractional abundance of HCO^+/HOC^+ dominates the breakdown diagram for CH_3OH with a BR value of 0.72.

It should be also noted that even at very large electron or photon energies, there is a fraction (about 16–20%) of methanol molecules that are ionized but survive fragmentation, leading to non zero $CH_3OH^{\bullet+}$ product detection at m/z = 32. For collisions with electrons from ∼60 up to 100 eV the BR for $CH_3OH^{\bullet+}$ remains constant at ∼0.20,[44] with a similar BR of 0.16 obtained for the dissociative photo-ionization at both 80[45] and 100[64] eV photon energies. This is different from the present study, where the methanol radical cation is never detected, thus indicating that collisions with $He^{\bullet+}$ lead to a greater degree of dissociation than those with either electrons or photons.

Another interesting comparison is with Li *et al.*,[65] who performed RRKM calculations to simulate relative product yields for fragmentation at different internal energies of the $CH_3OH^{\bullet+}$ radical cations. Calculations were reported at internal energies of 1.55, 3.10 and 4.64 eV and, at the highest energy, the HCO^+/HOC^+ channel is observed as the major one, with a BR = 0.68, a value that is not dissimilar to our findings.

3 Theoretical methodologies

We have performed a preliminary comparison between the experimental total CSs, measured as a function of the collision energy, with the predictions from traditional capture models. Such a comparison, given in Fig. 2, shows important inconsistencies between predictions and experimental findings. It is therefore necessary to develop a more detailed treatment of the interaction potential and of the collision dynamics. To this purpose, we provide, in analytical form, the multidimensional PES both in entrance and exit channels and adopt a treatment of the electron exchange process based on the Landau–Zener–Stückelberg approach. The relevant details of the theoretical methodologies exploited in this study are given in the following subsections.

3.1 Representation of the $[He–CH_3OH]^{\bullet+}$ interacting system

The geometry of the $[He–CH_3OH]^{\bullet+}$ complex is defined using a reference frame centered on the center of mass (CM) of the methanol molecule. The latter is subdivided into three constituent parts: the "effective atom" C_{eff}, which has the mass and the polarizability of a methyl group, the O atom and the H atom of the hydroxyl group. In particular, the polarizability of methanol, assumed equal to 3.21 Å^3,[66,67] is partitioned in three components, with 2.20 Å^3 assigned to C_{eff}, 0.76 Å^3 assigned to O and 0.25 Å^3 assigned to the hydroxyl H atom. The polarizability components obtained in this way are transferable values, *i.e.* they allow an evaluation of the polarizability of other molecules (for instance the dimethyl ether, previously investigated in ref. 37) in which methyl groups, H and/or O atoms are involved.

The geometrical parameters for methanol are derived through *ab initio* calculations, resulting in a value of 1.42 Å for the C–O bond length and 109.0° for the C_{eff}–O–H bond angle. In the adopted reference frame (see Fig. 3), the Cartesian coordinates (x, y, z) of the atoms in the methanol molecule are (in units of Å): O (−0.687, 0.096, 0), C_{eff} (0.729, −0.047, 0), H (−1.090, −0.777, 0). To simplify the mathematical description of the interaction potential, the geometries of reagents are expressed using spherical coordinates (R,θ,φ), where R is the distance connecting the center of mass of the methanol molecule with the position of the $He^{\bullet+}$ ion and θ defines the direction of the incoming ion. In particular, θ = 0° and 90°

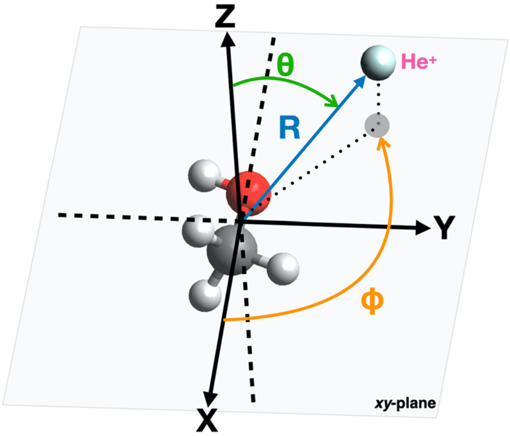

Fig. 3 Illustration of the coordinates and reference system used for the representation of the interaction potential between $He^{\bullet+}$ and CH_3OH.

correspond to $He^{\bullet+}$ approaching perpendicularly and along the xy plane, defined by the position of the O, H and C_{eff} groups. The angle φ specifies the projection of the R vector on the xy plane. An illustration of the coordinates used for the representation of the potential is reported in Fig. 3.

3.2 Entrance channel: $He^{\bullet+}$ + CH_3OH

The PES for the interaction of $He^{\bullet+}$ with CH_3OH is given as the sum of two different contributions: an electrostatic component, V_{elec}, and a non electrostatic component, V_{nelec}. V_{elec} is calculated considering the Coulomb interaction between $He^{\bullet+}$ and the effective charges residing on C_{eff}, O and H atoms. For CH_3OH, ElectroStatic Potential (ESP) derived atomic charges are obtained from *ab initio* calculations, using the B3LYP functional[68,69] in conjunction with the correlation consistent basis set aug-cc-pVTZ.[70,71] Using this formalism the total dipole moment for the methanol molecule is determined to be 1.700 Debye[66] and the resulting effective atomic charges are 0.2301e for C_{eff}, −0.6064e for O and 0.3762e for H atom, leading to an electrostatic term that can be expressed (in meV) as:

$$V_{\mathrm{elec}}(R,\theta,\varphi) = 14\,400 \times \left(-\frac{0.6064}{R_{\mathrm{O}}} + \frac{0.2301}{R_{\mathrm{C_{eff}}}} + \frac{0.3762}{R_{\mathrm{H}}}\right) \tag{10}$$

where R_O, $R_{C_{eff}}$ and R_H are the distances (in Å) between $He^{\bullet+}$ and O, C_{eff} and H atoms, respectively.

The V_{nelec} component is determined considering the combination between size repulsion contributions, operating at short distance, and induction and dispersion attraction contributions, operating at large intermolecular distances. Such contributions are expressed as a sum of three terms that account for the interaction of $He^{\bullet+}$ with the three effective atoms of the methanol molecule (C_{eff}, O and H). For each interaction pair the non electrostatic component is formulated by the Improved Lennard-Jones (ILJ) model,[72] which effectively describes both long-range and short-range interactions. The ILJ potential for a given interaction pair is given by the following equation:

$$V_{\mathrm{ILJ}}(r) = \varepsilon\left[\frac{m}{n(r)-m}\left(\frac{r_m}{r}\right)^{n(r)} - \frac{n(r)}{n(r)-m}\left(\frac{r_m}{r}\right)^{m}\right] \tag{11}$$

where r is the separation distance, while ε and r_m are the depth of the potential well and its location, respectively, associated to the interaction pair. The ratio r_m/r is hereafter referred to as reduced distance. For ion–neutral reactions the m parameter is equal to 4, while the $n(r)$ term depends on the hardness (β) of the two interacting fragments:

$$n(r) = \beta + 4\left(\frac{r}{r_m}\right)^2 \tag{12}$$

The overall non electrostatic component is then the sum of the three potentials:

$$V_{\mathrm{nelec}}(R,\theta,\varphi) = V_{\mathrm{ILJ}}(R_{\mathrm{C_{eff}}}) + V_{\mathrm{ILJ}}(R_{\mathrm{O}}) + V_{\mathrm{ILJ}}(R_{\mathrm{H}}) \tag{13}$$

Here a β value equal to 7 has been used for all the three interacting pairs, while the values of the other parameters are given in Table 3.

Table 3 List of the parameters used for the definition of the ILJ potential in the entrance and exit channel. The polarizability of $He^{\bullet+}$ is assumed to be ∼0.03 Å^3[36,37] and the value of ε and r_m parameters are obtained by correlation formulas representing the leading components of the intermolecular interaction in terms of polarizability components and charge of involved partners (see ref. 73 and references therein)

	Interacting pair	ε (meV)	r_m (Å)	m
Entrance	$He^{\bullet+}$–C_{eff}	312	2.58	4
	$He^{\bullet+}$–O	125	2.39	4
	$He^{\bullet+}$–H	76	2.05	4
Exit	He–C_{eff}	2.3	3.69	6
	He–O	1.7	3.38	6
	He–H	0.9	2.97	6

3.3 Exit channel: He + $CH_3OH^{\bullet+}$

The PES of the exit channel is comprised of a short range size repulsion and a long range attraction, with this latter term depending on the non-electrostatic contributions, *i.e.* induction (V_{ind}) and dispersion, with these two terms being similar in magnitude. The sum of the dispersion attraction and size repulsion effects is described as a van der Waals interaction, V_{vdW}, which is expressed, similarly to what already done for the entrance channel, in terms of three improved Lennard-Jones (ILJ) functions, one for each interaction pair:

$$V_{\mathrm{vdW}}(R,\theta,\varphi) = V'_{\mathrm{ILJ}}(R_{\mathrm{C_{eff}}}) + V'_{\mathrm{ILJ}}(R_{\mathrm{O}}) + V'_{\mathrm{ILJ}}(R_{\mathrm{H}}) \tag{14}$$

Here m has been fixed to 6, to correctly represent the asymptotic behaviour of the dispersion, while for β the value of 9 has been chosen for the three pairs due to the small "softness" of the He neutral partner. The parameters associated with the three different V'_{ILJ} contributions, together with the same V_{ILJ} terms for the entrance potentials are reported in Table 3.

The molecular ion is formed in an excited state, by ejection of one electron from an inner valence molecular orbital (MO) and its polarizability is assumed to be the same as that of the neutral methanol and is therefore partitioned in the same way.

An additional induction term represents the ion-induced dipole contribution, describing the interaction between the $CH_3OH^{\bullet+}$ radical cation and the He atom. The induction term V_{ind} (in meV) is expressed as a function of the polarizability of He (α_{He} = 0.2 Å^3) and the distance (R, in Å) between the two interacting partners, *via* the following expression:

$$V_{\mathrm{ind}}(R) = -7200\frac{\alpha_{\mathrm{He}}}{R^4} \tag{15}$$

where the factor 7200 provides the long range C_4 (charge-induced dipole attraction coefficient) in meV Å^4 units. The basic features of the resultant multidimensional PESs, controlling the entrance and exit channel dynamics, are reported in the next section.

3.4 Crossing points between entrance and exit channels

The collisional energy of the present experiment, spanning a range from ∼0.04 to 10 eV, allows for a non-adiabatic transition located at the crossing between the entrance and the exit PESs. Nevertheless, the difference in the ionization energy (IE) of the two species (24.59 eV for He and 10.84 eV for CH_3OH[74]) does not allow a crossing between entrance and exit channel in the case of an electron ejected by the HOMO of the methanol molecule.

In order to have a crossing between the entrance and the exit potentials, the electron must be removed from an inner valence molecular orbital, with a high ionization potential. The calculated electronic configuration for methanol is $(1a')^2\ (2a')^2\ (3a')^2\ (4a')^2\ (5a')^2\ (1a'')^2\ (6a')^2\ (7a')^2\ (2a'')^2$. According to previous investigations the experimental ionization energy of the inner valence orbital 4a′ (representing the HOMO−5 orbital) is 22.65 eV,[75] in good agreement with a recent re-evaluation which gave a value of 22.623 eV,[76] enough to promote the electron transfer process. Note that the other molecular orbitals of CH_3OH have ionization energies that are too low with respect to the recombination energy of $He^{\bullet+}$, thus giving either no crossings between the entrance and exit PES or crossings that are not accessible within the collision energy range probed in the present experiments. The PES for the exit channel can be rescaled considering the value of IE of the 4a′ orbital, allowing for the identification of a crossing point between the entrance and the scaled exit potentials.

In Fig. 4 the curves obtained by PES cuts at four different configurations are shown. For each configuration three curves are reported, representing the entrance (green), exit (red) and scaled exit potentials (red-dashed) resulting from the removal of an electron from the inner 4a orbital. The zero of the energy scale is taken to coincide with the value at $R \to \infty$ of the PES of the entrance channel. For one of the most attractive configurations (*e.g.* $\theta = 90°$ and $\varphi = 135°$, see left upper panel of Fig. 4), one relevant crossing point between the entrance and the exit curves is located at $R = 2.464$ Å. For unfavourable configurations (*e.g.* $\theta = 90°$ and $\varphi = -45°$, $-90°$ and $-135°$, see the other three panels in Fig. 4) the crossing points are either not present or inaccessible since they are too high in energy.

In order to properly evaluate the occurrence probability of the electron transfer process, the electron density distribution of methanol must be taken into account. For this reason, electronic structure calculations were performed at the B3LYP/aug-cc-pVTZ level of theory in order to obtain the electron density map of the 4a′ (HOMO−5) molecular orbital, shown in Fig. 5, directly involved in the electron transfer to $He^{\bullet+}$.

3.5 The Landau–Zener–Stückelberg treatment extended to dissociative electron exchange reactions

The transition probability at the crossing point between the two curves is treated by adopting the same strategy successfully used in previous investigations.[37,77,78] More specifically, the Landau–Zener–Stückelberg approach[79–81] is used for the implementation of a one-dimensional model, that considers specific slices of the multidimensional PES at fixed values of θ and φ as a function of the reaction coordinate R. The CS for the electron

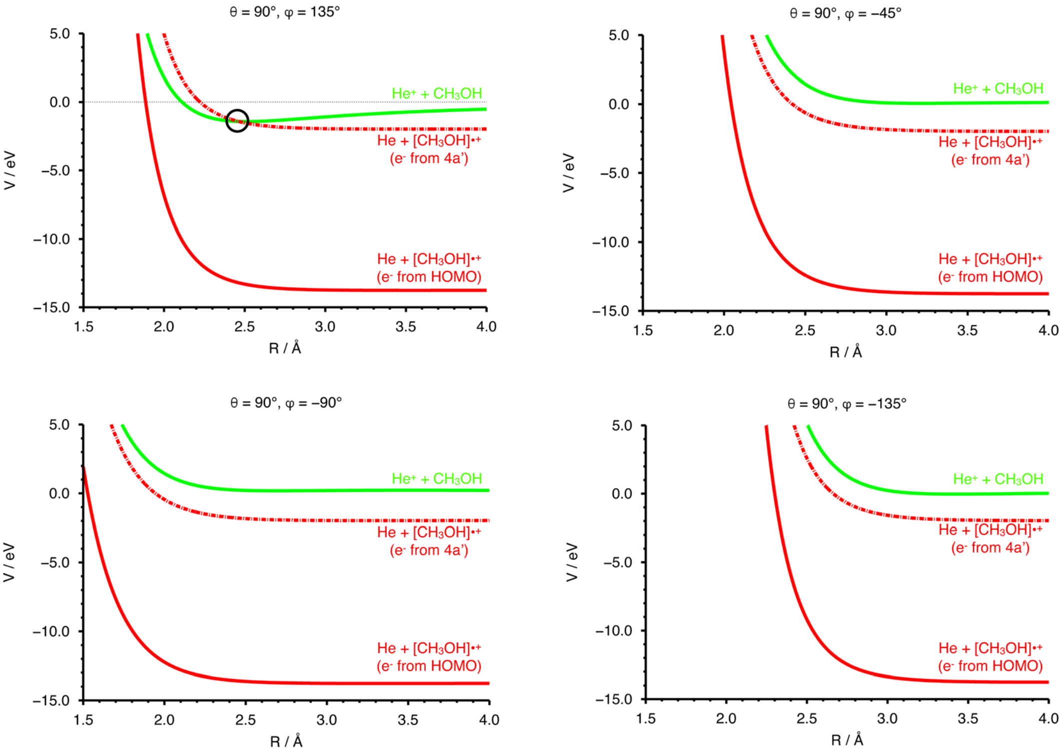

Fig. 4 Left upper panel: PES curves for the entrance (green) and exit channels (red) at fixed values of $\theta = 90°$ and $\varphi = 135°$. The exit curves, considering an electron removed from the HOMO and from the HOMO−5 (4a′) orbitals, are reported as solid and dashed lines, respectively. The other three panels emphasize the absence of the crossing with the exit channels for configurations (top right: $\theta = 90°$ and $\varphi = -45°$; bottom left: $\theta = 90°$ and $\varphi = -90°$; bottom right: $\theta = 90°$ and $\varphi = -135°$) of the precursor state in the entrance channels where the repulsion due to strongly anisotropic electrostatic effects dominate. The zero energy is the same in all cases and further details on the PES anisotropy are given Section 4.2.

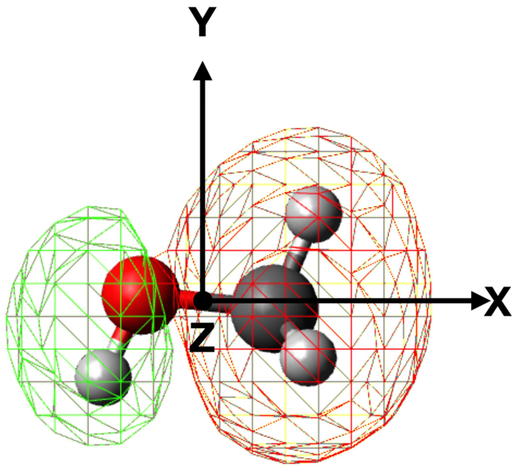

Fig. 5 Electron density map of the 4a′ (HOMO−5) inner valence molecular orbital of neutral methanol.

exchange process is calculated considering a cone of configurations with θ and φ values around 90° and 120°, respectively. The probability of passage through a crossing between the two curves is given by:

$$p_i(E,\theta,\varphi,l) = \exp\left(\frac{-2\pi H_i^2}{\hbar v_R(l,E)\Delta_i}\right) \qquad (16)$$

where E and l are the collision energy and the quantum number describing the orbital angular momentum of the collision complex, respectively, while H_i represents the non-adiabatic coupling between the two curves and Δ_i is the difference in slope between the entrance and exit curves at the crossing point. The radial velocity v_R is defined as:

$$v_R{}^2 = \frac{2}{\mu}\left[E\left(1-\frac{l(l+1)}{k^2R_i^2}\right)-E_i\right] \qquad (17)$$

where E_i and R_i are the values of energy and R at the crossing point, respectively. The total integral CS for the electron transfer is considered as a sum of contributions for each value of l:

$$\sigma(E,\theta,\varphi) = \frac{\pi}{k^2}\sum_{l=0}^{l_{\max}}(2l+1)P_i(E,\theta,\varphi,l) \qquad (18)$$

where the probability of formation of $CH_3OH^{\bullet+}$ ($P_i(E,\theta,\varphi,l)$) is expressed in terms of the previously described $p_i(E,\theta,\varphi,l)$. The sum in eqn (18) extends up to $l_{\max}$, the maximum value of l for which the system is able to overcome the centrifugal barrier to reach the crossing point located at R_i. For high collision energies $l_{\max}$ is given by the maximum value of l for which v_R is real, namely:

$$l_{\max} = kR_i\sqrt{1-\frac{E_i}{E}} \qquad (19)$$

According to the guidelines discussed in ref. 37, for low collision energies the $l_{\max}$ value should be reduced to avoid the non-physical condition of a centrifugal barrier in the entrance channel higher than the available collision energy. Such a limitation in the $l_{\max}$ leads to smaller CSs for collision energies smaller than ∼100 meV.

Applying the same criteria as discussed in ref. 36 and 37, P_i can be here represented as:

$$P_i = (1 - p_i)(1 + p_i) \qquad (20)$$

It should be noted that any orientation dependence of P_i appears indirectly in the evaluation of the crossing position and of the radial velocity.

3.6 Potential energy surface for the dissociation process

The energetics and fragmentation pathways of $CH_3OH^{\bullet+}$ radical cation are investigated through *ab initio* calculations. The analysis of the Potential Energy diagram for the dissociation of $CH_3OH^{\bullet+}$, starting from its ground electronic state, is performed adopting a computational strategy successfully used in the past for the investigation of several processes.[82–84] Calculations start with optimization of the geometry of all identified stationary points in the PES by means of Density functional theory (DFT). In the present work, geometry optimization has been performed using two different functionals: B3LYP and ωB97X-D,[85] both in in conjunction with the correlation consistent basis set aug-cc-pVTZ.

Harmonic vibrational frequencies are evaluated, at the same level of theory, in order to identify the nature of each stationary point, *i.e.* minimum if all the frequencies are real and transition state if there is one, and only one, imaginary frequency. Subsequently, the energies of all the stationary points are evaluated at an higher level of theory, *i.e.* CCSD(T)[86–88]/aug-cc-pVTZ. The zero-point energy corrections, evaluated at the B3LYP/aug-cc-pVTZ level or at the ωB97X-D/aug-cc-pVTZ level, are then added to the CCSD(T) energies to obtain values at 0 K. All calculations are performed using Gaussian09,[89] while the frequencies analysis is performed using AVOGADRO.[90] Results of the calculations employing the ωB97X-D functional are reported in the next Section, where they are also compared with existing literature values. Complementary data extracted from the B3LYP calculations are listed in the ESI.†

4 Results and discussion

4.1 Potential energy surface for the dissociation process

The $CH_3OH^{\bullet+}$ cation, formed directly after the electron transfer to $He^{\bullet+}$, possesses a high degree of internal energy. As a consequence, a fast electronic rearrangement is expected, leading to instantaneous dissociation. The PES for the dissociation of the $CH_3OH^{\bullet+}$ cation from its ground electronic state is reported in Fig. 6. The calculated energies (at the CCSD(T)/aug-cc-pVTZ//ωB97X-D/aug-cc-pVTZ level) are reported considering the $CH_3OH^{\bullet+}$ cation as reference (with energy of 0.0 eV).

Once formed, the aforementioned cation can directly dissociate leading to the formation of six different combinations of products. The breaking of the C–O bond leads to the formation of the OH radical plus the $CH_3{}^+$ cation, with a relative energy of 2.78 eV, in a barrierless process. Another process with no energy barrier is H atom elimination, leading

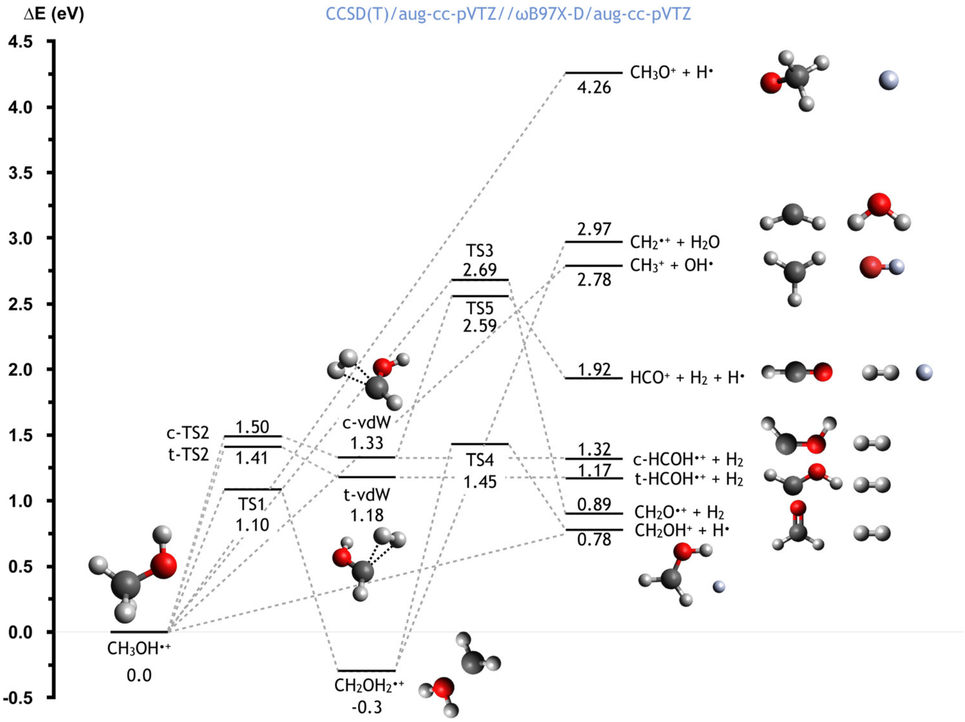

Fig. 6 Schematic representation of the PES for the dissociation of the $CH_3OH^{\bullet +}$ cation, with the energies (reported in eV) evaluated at the CCSD(T)/aug-cc-pVTZ//ωB97X-D/aug-cc-pVTZ level of theory. A similar figure with the energies computed at the CCSD(T)/aug-cc-pVTZ//B3LYP/aug-ccpVTZ level is reported in the ESI.†

to the concominant formation of the CH_3O^+ cation, with an endothermicity of 4.26 eV. Four different processes lead to the formation of molecular hydrogen. Firstly, the co-ejection of the H atom of the hydroxyl group with one of the three methyl hydrogens leads to the formation of $CH_2O^+ + H_2$, with an overall energy of 0.89 eV, and a barrier, TS3, of 2.69 eV. Alternatively, the elimination of two methyl hydrogens first leads to the formation of *cis*/*trans* van der Waals complexes (indicated as *c*-vdW and *t*-vdW in Fig. 6), which are higher in energy by 1.33 and 1.18 eV respectively. In the case of *c*-vdW, the subsequent breaking of the O–H bond can lead to the formation of $HCO^+ + H_2 + H$. This has an overall endothermicity of 1.92 eV with a barrier of 2.59 eV (*via* TS5). Without cleavage of the O–H bond, *c*-vdW and *t*-vdW lead to *cis*- and *trans*-$HCOH^+ + H_2$, with reaction energies of 1.32 and 1.17 eV respectively.

An alternative reaction mechanism is the isomerization of $CH_3OH^{\bullet +}$ *via* an 1,2 H-shift, leading to the formation of $CH_2OH_2^+$, with a reaction energy of −0.30 eV and a barrier of 1.10 eV (*via* TS1). The resultant cation can dissociate, *via* a barrier located 1.45 eV above the zero energy (TS4), to give $H + CH_2OH^+$, with a reaction energy of 0.78 eV (relative to $CH_3OH^{\bullet +}$). Alternatively, the cleavage of the C–O bond leads to the formation of water, together with the CH_2^+ cation, in a barrierless process with a reaction energy of 2.97 eV (relative to $CH_3OH^{\bullet +}$).

Importantly, this PES describes the fragmentation of ground state $CH_3OH^{\bullet +}$ whereas, as can be the case in the reaction studied in this work, the removal of an electron from an inner molecular orbital leads to the formation of $CH_3OH^{\bullet +}$ in an excited state. This therefore means that, though some of these channels are endothermic in the case of the ground state, all are accessible for the excited state.

Several theoretical investigations have been performed in the recent years in order to properly understand the fragmentation pathways of the $CH_3OH^{\bullet +}$ cation.[91–93] To the best of our knowledge, the first theoretical investigation goes back to 1991, when Ma *et al.*[93] analyzed the main isomerization and fragmentation pathways of ionized methanol, leading to two main product channels: $HOC^+ + H_2 + H$ and $HCO^+ + H_2 + H$. These authors identified different long range interacting complexes, relevant to the formation of H_2, which interacts with the remaining co-fragment prior to its elimination. More accurate CCSD(T)/cc-pVTZ//B3LYP/6-311++G(d,p) calculations have been performed by Wu *et al.*,[92] revealing the possible formation of other important species, including H_3/H_3^+ and $CH_2^+ + H_2O$. Finally, *Li et al.*[91] reported a complete investigation of the global PES for the fragmentation of $CH_3OH^{\bullet +}$ using both DFT theory (B3LYP/6-311G(d,p)) and more accurate G3(MP2,CCSD) methods for energy evaluations. Different product channels have been identified, leading to the formation of H, OH, H_2O and H_2 as neutral co-fragments. In the present work we performed a new evaluation of the stationary points on the fragmentation PES in order to provide a global picture of all the possible product channels to assist the interpretation of experimental results.

4.2 Potential energy surface and dynamics of the electron transfer process

The initial approach of $He^{\bullet +}$ towards methanol has been simulated from multiple directions by varying the cation's

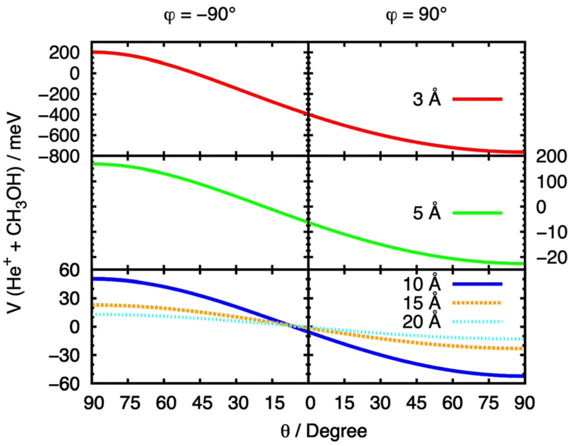

Fig. 7 Cuts of the PES for the entrance channel of the $He^{\bullet+}$ + CH_3OH system for φ = 90° and φ = −90° considering the variation of θ at fixed values of R.

spherical coordinates θ and φ. From here on, we refer to each θ and φ pair as a "configuration" of the system. In order to fully understand the effect of the orientation of the two interacting partners on the entrance potential, the PES has been calculated at a set of fixed distances for different values of θ. At R values corresponding to 3, 5, 10, 15 and 20 Å the entrance potential has been evaluated at $\varphi = -90°$ and 90° over a range of θ angles between 0° and 90°. A slice of the entrance channel PES is reported in Fig. 7, where a strong repulsive potential is present at $\varphi = -90°$, corresponding to $He^{\bullet+}$ approaching the H atom of the OH group. The potential appears to be attractive when the $He^{\bullet+}$ approaches the region of OH group (φ = 90°), due to a strong effect of the electrostatic component of the interaction. A minimum in the potential is observed at $\theta \approx 90°$, a configuration in which the ion is located in the same plane as the C_{eff}–O–H atoms of the molecule.

In Fig. 8, a similar procedure has been applied, with the same set of fixed R values, to the θ = 90° case, in order to evaluate the effect of the variation of the angle φ on the entrance potential. In this case, a minimum in the potential is observed at 90° ≤ φ ≤ 150°, which corresponds to a configuration in which the ion approaches the O atom.

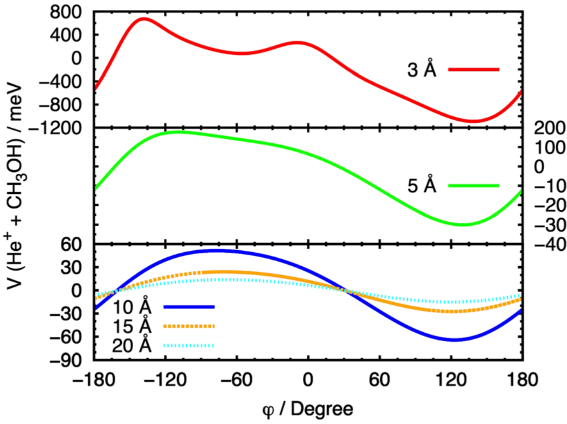

Fig. 8 Cuts of the PES for the entrance channel of the $He^{\bullet+}$ + CH_3OH system for θ = 90° considering the variation of φ at fixed values of R.

This is further illustrated in Fig. 9, where the PES for the approach of the ion in the xy plane (*i.e.* with θ = 90° and −180° ≤ φ ≤ 180°) has been presented in a three-dimensional plot, with the attractive and repulsive contributions being represented by blue and yellow, respectively. The figure shows that, due to the polarity of the methanol molecule, the entrance channel PES is strongly anisotropic. For this reason, it is expected that the reagents, during their approach, tend to assume spontaneously the most attractive configuration, especially under sufficiently long collision times.

In addition to the relative orientation in the entrance channel, the position and energy of crossing(s) between the entrance and exit channels also needs to be investigated. In Fig. 4 (left upper panel) we have selected the configuration (θ = 90°, φ = 135°) for which the entrance PES as a function of R shows a deep potential well. In the same panel of Fig. 4 the exit PES has been reported for the same configuration, rescaled by the IE value of the 4a molecular orbital of CH_3OH, to represent the removal of the electron from this inner molecular orbital. The resulting crossing point is located at a distance between $He^{\bullet+}$ and the center of mass of the methanol molecule of 2.462 Å, with V = −1.419 eV. Hence, for this configuration, an exothermic crossing can occur, and similar behaviours is expected for other configurations. The strong anisotropy of the PES is expected to have an effect on the electron transfer process. In particular, assuming that the most attractive configurations lead to a significant contribution to the CS, only select configurations drive the charge exchange process, namely those corresponding to the approach of $He^{\bullet+}$ towards the oxygen side. As a consequence the reaction probability is only non-zero for a select set of configurations.

4.3 Electron transfer cross sections

The calculation of the electron transfer CSs have been performed using two different approaches to account for the two different dynamical collision regimes.

(i) Isotropic model. In the first case calculations have been performed assuming a statistical distributions of relative orientations of reagents. Total CSs calculated by averaging CSs over an appropriate number of (θ, φ) couples account for the role of different, but equally probable, directions of approach for $He^{\bullet+}$ towards CH_3OH, regardless of relative orientation. CS calculations have been performed by averaging over a total of 128 configurations and the choice of the non-adiabatic coupling term, at the crossing point i between entrance and exit reaction channels, has been made under the criteria discussed in detail later on in this Section. The results, presented in Fig. 10 as a green dashed line, clearly underestimate the experimental data at all probed collision energies (with the exception of few data points at the upper limit of the experimental collision energy range).

This disagreement represents a robust indication that the adopted assumption is unsatisfactory and that the dynamical treatment must take into account the role played by the strong

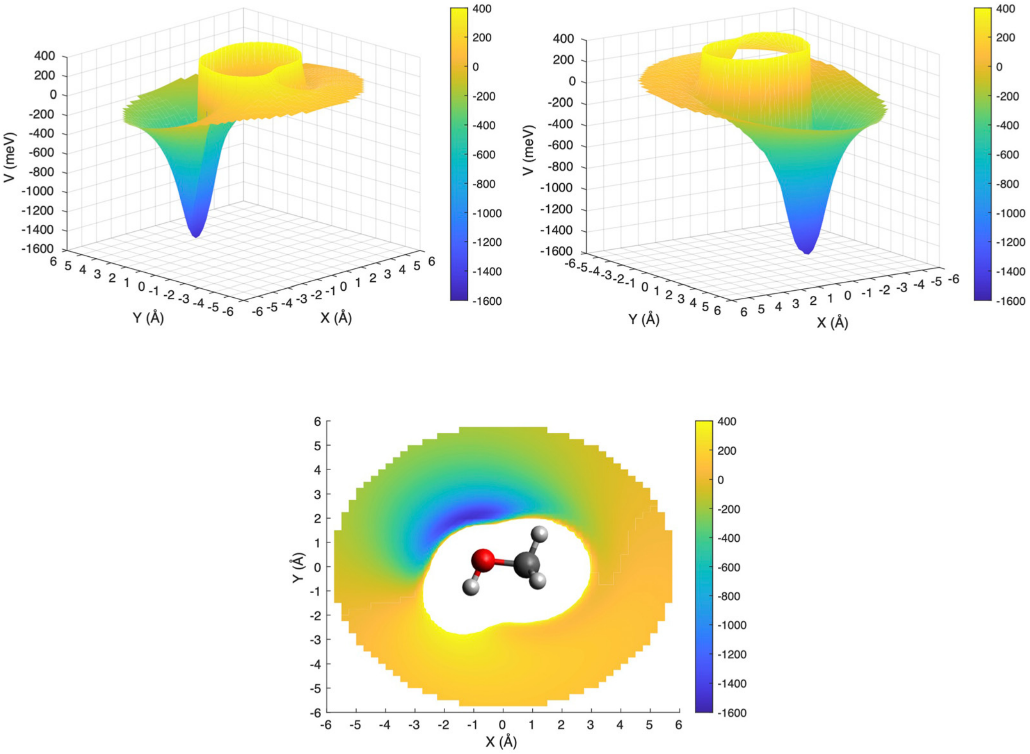

Fig. 9 3D PES for the entrance channel with the attractive and repulsive contributions reported in blue and yellow, respectively.

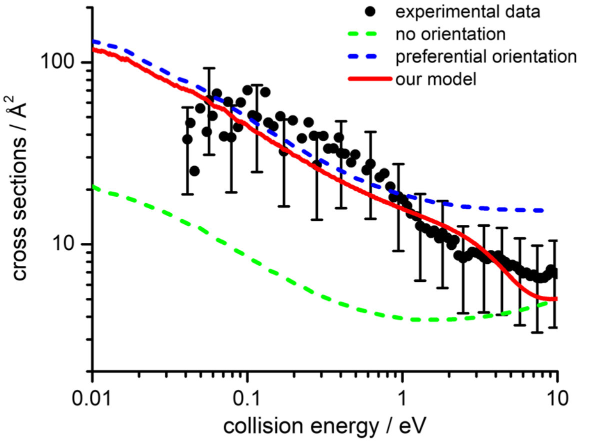

Fig. 10 Comparison of experimental (black filled circles) and computed total CSs according to the theoretical treatment described in the text and based on an improved Landau–Zener–Stückelberg approach: isotropic model (green dashed line), preferential orientations (blue dashed line), weighted sum (red line).

anisotropy of the PES on the reagents side, which tends to channel the approaching particles in specific relative configurations. In particular, as observed in similar systems previously investigated with the same technique,[36,37] in the strong electric field generated by the very small He$^{\bullet+}$ ions, the anisotropic molecule will seek to orient its dipole moment around the configuration of minimum energy.

(ii) Preferential orientations. The second approach assumes that at the asymptote, where the interaction potential energy tends to zero, the CH_3OH molecule is free to rotate (the mean rotational energy of CH_3OH is ~40 meV at $T = 300$ K). However, as the colliding partners approach, the rotation of polar CH_3OH becomes either partially or totally hindered by the intermolecular electric field gradient associated with the interaction anisotropy. As a consequence, in the reference frame adopted to describe the dynamics, the rotational motion of CH_3OH decreases as the system climbs the repulsive wall of the PES and increases in the other half-turn due to the attraction. This effect becomes more prominent at short separation distances, where the PES anisotropy is larger.

As can be observed in Fig. 8, the energy barriers arising from the interaction anisotropy become comparable to the mean rotational energy of CH_3OH at $R \sim 15$ Å. However, at shorter distances, the barrier that inhibits the rotation becomes insurmountable and the molecule librates like a pendulum around the position of minimum energy. In this case, the collision system is confined in a so-called *pendular state*, in which molecular rotations are transformed into bending vibrations of the collision complex (for further details see Fig. 6 of ref. 36). As the distance decreases, so does the amplitude of the oscillation, and eventually the molecule is locked in its preferential orientation.

Orientation effects of this type become increasingly efficient at low collision energies, as the collision time becomes sufficiently long with respect to the rotational period of the molecule. They can influence the dynamics of the electron exchange process by channelling most of the trajectories in narrow angular cones confined around the most attractive configurations of the intermolecular interaction (see Fig. 7–9). Considering that the most attractive geometries are the least efficient for the electron transfer process, when the extension and symmetry of the molecular orbitals involved in the electron exchange are taken into account, the reaction can essentially be promoted by the coupling between the rotational angular momentum of nuclei in the complex and the orbital angular momentum of the electrons (Coriolis coupling).

To evaluate the magnitude of the coupling and to account for its orientation dependence, the modelling was properly extended to include the change with E of the original orientation in the collision complex. In particular, the coupling is expected to be less efficient when reagent molecules are strongly oriented. Following the guidelines given in ref. 37, the Landau expression for the coupling has been adopted:

$$H_i(l, E, \theta, \varphi) = \frac{\hbar l}{\mu R_i^2} M \tag{21}$$

In the above equation the M term has been extended as:

$$M = C\left|\frac{E}{E_i}\right|^{\frac{1}{4}} \tag{22}$$

where, as already defined, E is the collision energy and E_i is the energy value of the crossing point i. In the present investigation the C value is set to $C = 4$ in order to reproduce the absolute value of measured total ionization CS in the intermediate and low E range probed experimentally (see blue dashed line in Fig. 10).

At the higher collision energies ($E \geq 4$ eV) the collision time decreases and so the reorientation of CH_3OH towards the most attractive configurations is expected to be infeasible. To account for this we have assumed that, in the collision energy range $2 \leq E \leq 4$ eV, a dynamic regime that encompasses both effects is required to reproduce the experimental data. Accordingly, the collision energy dependence of the total ionization CS $\sigma_t(E)$ has been calculated as a weighted sum of $\sigma_{\mathrm{cone}}(E)$ and of $\sigma_{\mathrm{sphere}}(E)$:

$$\sigma_t(E) = \sigma_{\mathrm{cone}}(E) f_0(E) + \sigma_{\mathrm{sphere}}(E)(1 - f_0(E)) \tag{23}$$

where f_0 is a Fermi weight function, expressed as:

$$f_0(E) = \frac{1}{1 + e^{\frac{E - E_0}{E_t}}} \tag{24}$$

The values of E_0 and E_t factors define, respectively, the E values at which the two limiting regimes of the collision dynamics exhibit the same weight and how fast the passage between the two calculation methods occurs. In the present study E_0 and E_t have been selected, respectively, in the range of 3.0 and 1.5 eV and the so calculated CS are reported as red line in Fig. 10. From this it can be seen that at low collision energies (when $E_{\mathrm{CM}} < \sim 1.5$ eV) the preferential orientations model effectively fits the experimental results, while at higher energies ($E_{\mathrm{CM}} > 5$ eV) the isotropic model better reproduces the absolute value of CS. As a result, at higher collision energies the strong stereodynamical effect tends to vanish.

Observed stereo-dynamical effects indicate that for several configurations, defined in a statistical way by the isotropic model, the crossing points are either not present or energetically inaccessible since they are too high in energy. In addition, for some configurations, the turning points (the distance of closest approach of reagents) are too external with respect to the crossing points opening the charge exchange channel. Such crossing points become accessible only at very high collision energies, probing shorter intermolecular distances.

4.4 Cross sections and rate coefficients: comparison with previous models

CSs and rate coefficients for ion–molecule reactions, with their dependence on energies/temperature, are usually evaluated using various types of capture models (see ref. 94 for a very recent review). For the system here presented such models are unable to correctly describe the absolute values and the collision energy dependence of CSs, measured under thermal and hyper-thermal conditions. In particular, at a collision energy of 60 meV (confined in the thermal range) the CS predicted by classical capture models is a factor 5–7 larger respected to the measured value (see Fig. 2).

The present treatment, adopted to correctly reproduce the experimental findings, suggests that observed deviations from predictions of capture models are representative of stereo-dynamical effects, ascribed to the strong interaction anisotropy in the entrance channel of the reaction. Such anisotropic interactions lead to the formation of a precursor state, localized at short intermolecular distances, in specific configurations. Moreover, the symmetry of molecular orbital, of relevance for the chemical forces involved in the electron exchange, at the PE curves crossings, further controls the selectivity of the process. Such stereo-dynamical effects are expected to play an increased role also under sub-thermal conditions, because the increase of the collision time favours the formation of the precursor state in its most stable configurations.

From the CSs obtained using the improved Landau–Zener–Stückelberg method described in the previous section (namely the red line from Fig. 10), it is possible to evaluate the reaction rate coefficient as a function of temperature ($k(T)$) in the thermal and hyper-thermal range and to attempt an extrapolation under sub-thermal conditions. The $k(T)$ can be calculated by averaging the computed total integral cross section over a Maxwell-Boltzmann distribution of collision energies, following the definition of rate constant in collision theory in chemical kinetics (see for instance Section 1.2.5 of ref. 95 and 35).

At 300 K our model gives an estimated rate coefficient of 1.0×10^{-9} cm^3 s^{-1}, which is smaller than the values from KIDA[33] ($k = 4.8 \times 10^{-9}$ cm^3 s^{-1} from classical trajectory scaling method of Su and Chesnavich[52,96,97]) and UDfA[34] ($k = 2.2 \times 10^{-9}$ cm^3 s^{-1}). When we attempt an extrapolation at the low temperatures relevant for interstellar conditions ($\sim$10 K) our estimated rate is about a factor 10–30 lower respect to KIDA value ($k = 2.0 \times 10^{-8}$ cm^3 s^{-1} at 10 K[33]) and to the long range transition state theory model of Georgievskii and Klippenstein[98] that estimates a $k = 2.3 \times 10^{-8}$ cm^3 s^{-1} at 10 K.

Present and previous results,[35] obtained with the same methodology, raise the important question that capture models, extensively used to describe ion-molecule reactions, can exhibit a different degree of reliability, depending on the specific features of the reagents. This represents a crucial problem to collect reliable/accurate rate coefficients for plasmas and astrochemical databases. In our opinion this open question can be properly addressed by performing, under the same conditions, additional experiments extended at low collision energies (*i.e.* below 0.05 eV, that are unfortunately unfeasible using our experimental set-up), in order to provide internally consistent data for different ion-molecule reactions.

5 Conclusions/summary

- We have reported measurements of the absolute cross sections (CSs) and branching ratios (BRs) for the collisions of $He^{\bullet+}$ ions with CH_3OH as a function of the collision energy, in the range from ∼0.04 to ∼10 eV.
- A striking difference is observed between our experimental BRs and the estimates reported in astrochemical databases. In both cases the electron exchange process is completely dissociative; but while databases indicate a BR of 0.50 for the two channels CH_3^+ plus OH and OH^+ plus CH_3, our results, summarized in Table 2, show that the most abundant fragment is HCO^+/HOC^+ with a BR equal to 0.74 ± 0.18, the CH_3^+ fragment is the second most abundant (with BR = 0.10 ± 0.03) and the OH^+ fragment is not detected.
- A theoretical interpretation in support of experimental results is proposed, based on analytical expressions for the entrance and exit multidimensional PESs, and on the modelling of non-adiabatic transitions *via* a Landau–Zener–Stückelberg approach, to estimate transition probabilities at crossings between diabatic curves.
- In addition to all constraints of traditional capture methods, the present treatment encloses: (i) the definition of a separation distance range where charge transfer coupling manifests. This information, together with the role of centrifugal barrier in the entrance channels, selects the l values effectively triggering the reaction; (ii) the indication of the molecular orbitals involved in the electron transfer process; (iii) the structure and stability of the precursor state more efficiently formed by collisions at each l value.
- The collision dynamics is treated within a semiclassical method, expected to be quantitative for collision energies larger than 1 meV (∼10 K) and semi-quantitative for lower energies, where quantum effects may become prominent.
- It is shown that the (diabatic) reactant surface does not cross the product surface that correlates asymptotically with the ground state of $CH_3OH^{\bullet+}$. Crossing is possible only assuming that the electron is removed by an inner valence orbital (namely the 4a′ having a vertical ionization energy ∼11.67 eV higher than the HOMO), thus the nascent radical cation is formed in a highly excited state that quickly dissociates.
- To reproduce experimental findings a strong orientation effect of the polar CH_3OH molecule in the electric field generated by $He^{\bullet+}$ should be assumed. This is a general result and points to the fact that stereo-chemical effects should not be disregarded when seeking to obtain reasonable estimates of dynamical processes. For recent examples of the influence of stereochemical effects on the reactivity of other ion–molecule systems at low and ultra low collision energies see for instance.[99–105]
- The experimental CSs and product BRs here reported should be used when modelling the abundance of the ubiquitous methanol molecule in the interstellar medium, with special reference to those regions where collisions with $He^{\bullet+}$ are expected to be among the main destruction routes.

Conflicts of interest

There are no conflicts to declare.

Acknowledgements

This project has received funding from the European Unions Horizon 2020 research and innovation programme under the Marie Sklodowska Curie grant agreement no. 811312 for the project ''Astro-Chemical Origins'' (ACO) and from MUR PRIN 2020 project n. 2020AFB3FX ''Astrochemistry beyond the second period elements''. The authors thank the Herla Project (**http://www.hpc.unipg.it/hosting/vherla/vherla.html**) – Universit'a degli Studi di Perugia for allocated computing time. The authors thank the Dipartimento di Ingegneria Civile ed Ambientale of the University of Perugia for allocated computing time within the project ''Dipartimenti di Eccellenza 2018–2022''. N. F.-L. thanks MUR and the University of Perugia for the financial support of the AMIS project through the ''Dipartimenti di Eccellenza'' programme. N.F.-L. also acknowledges the Fondo Ricerca di Base 2021 (RICBASE2021FAGINAS) del Dipartimento di Chimica, Biologia e Biotecnologie della Universit'a di Perugia for financial support. We are grateful to Prof. Paolo Tosi (Depart. Physics, University of Trento) for useful discussions and to Mr Damiano Avi for technical assistance during the experiments.

Notes and references

1 E. Herbst and E. F. van Dishoeck, *Annu. Rev. Astron. Astrophys.*, 2009, **47**, 427–480.
2 S. A. Sandford, M. Nuevo, P. P. Bera and T. J. Lee, *Chem. Rev.*, 2020, **120**, 4616–4659.
3 J. K. Jorgensen, A. Belloche and R. T. Garrod, *Annual Review of Astronomy and Astrophysics,* ed. E. VanDishoeck and R. Kennicutt, 2020, vol. 58, pp. 727–778, DOI: 10.1146/annurev-astro-032620-021927.
4 K. I. Oberg and E. A. Bergin, *Phys. Rep.*, 2021, **893**, 1–48.
5 J. A. Ball, C. A. Gottlieb, A. E. Lilley and H. E. Radford, *Astrophys. J.*, 1970, **162**, L203.
6 S. Spezzano, A. Fuente, P. Caselli, A. Vasyunin, D. Navarro-Almaida, M. Rodriguez-Baras, A. Punanova, C. Vastel and V. Wakelam, *Astron. Astrophys.*, 2021, **657**, A10.

7 C.-F. Lee, Z.-Y. Li, P. T. P. Ho, N. Hirano, Q. Zhang and H. Shang, *Astrophys. J.*, 2017, **843**, 27.

8 A. Belloche, A. J. Maury, S. Maret, S. Anderl, A. Bacmann, P. Andre, S. Bontemps, S. Cabrit, C. Codella, M. Gaudel, F. Gueth, C. Lefevre, B. Lefloch, L. Podio and L. Testi, *Astron. Astrophys.*, 2020, **635**, A198.

9 Y.-L. Yang, N. Sakai, Y. Zhang, N. M. Murillo, Z. E. Zhang, A. E. Higuchi, S. Zeng, A. Lopez-Sepulcre, S. Yamamoto, B. Lefloch, M. Bouvier, C. Ceccarelli, T. Hirota, M. Imai, Y. Oya, T. Sakai and Y. Watanabe, *Astrophys. J.*, 2021, **910**, 20.

10 L. Chahine, A. Lopez-Sepulcre, R. Neri, C. Ceccarelli, S. Mercimek, C. Codella, M. Bouvier, E. Bianchi, C. Favre, L. Podio, F. O. Alves, N. Sakai and S. Yamamoto, *Astron. Astrophys.*, 2022, **657**, A78.

11 S. Mercimek, C. Codella, L. Podio, E. Bianchi, L. Chahine, M. Bouvier, A. Lopez-Sepulcre, R. Neri and C. Ceccarelli, *Astron. Astrophys.*, 2022, **659**, A67.

12 M. De Simone, C. Codella, C. Ceccarelli, A. Lopez-Sepulcre, A. Witzel, R. Neri, N. Balucani, P. Caselli, C. Favre, F. Fontani, B. Lefloch, J. Ospina-Zamudio, J. E. Pineda and V. Taquet, *Astron. Astrophys.*, 2020, **640**, A75.

13 C. Walsh, R. A. Loomis, K. I. Oberg, M. Kama, M. L. R. van't Hoff, T. J. Millar, Y. Aikawa, E. Herbst, S. L. W. Weaver and H. Nomura, *Astrophys. J. Lett.*, 2016, **823**, L10.

14 M. L. R. van't Hoff, J. J. Tobin, L. Trapman, D. Harsono, P. D. Sheehan, W. J. Fischer, S. T. Megeath and E. F. van Dishoeck, *Astrophys. J. Lett.*, 2018, **864**, 23.

15 L. Podio, A. Garufi, C. Codella, D. Fedele, E. Bianchi, F. Bacciotti, C. Ceccarelli, C. Favre, S. Mercimek, K. Rygl and L. Testi, *Astron. Astrophys.*, 2020, **642**, L7.

16 N. van Der Marel, A. S. Booth, M. Leemker, E. F. van Dishoeck and S. Ohashi, *Astron. Astrophys.*, 2021, **651**, L5.

17 A. S. Booth, C. Walsh, J. Terwisscha van Scheltinga, E. F. van Dishoeck, J. D. Ilee, M. R. Hogerheijde, M. Kama and H. Nomura, *Nat. Astronomy*, 2021, **5**, 684–690.

18 L. Le Roy, K. Altwegg, H. Balsiger, J.-J. Berthelier, A. Bieler, C. Briois, U. Calmonte, M. R. Combi, J. De Keyser, F. Dhooghe, B. Fiethe, S. A. Fuselier, S. Gasc, T. I. Gombosi, M. Haessig, A. Jaeckel, M. Rubin and C.-Y. Tzou, *Astron. Astrophys.*, 2015, **583**, A1.

19 M. Rubin, D. Bekaert, V. M. W. Broadley, M. N. Drozdovskaya and S. F. Wampfler, *ACS Earth Space Chem.*, 2019, **3**, 1792–1811.

20 K. Altwegg, H. Balsiger and S. A. Fuselier, in *Annual Review of Astronomy And Astrophysics*, ed. S. Faber, E. VanDishoeck and R. Kennicutt, 2019, vol. 57, pp. 113–155.

21 W. M. Grundy, M. K. Bird, D. T. Britt, J. C. Cook, D. P. Cruikshank, C. J. A. Howett, S. Krijt, I. R. Linscott, C. B. Olkin, A. H. Parker, S. Protopapa, M. Ruaud, O. M. Umurhan, L. A. Young, C. M. D. Ore, J. Kavelaars, J. T. Keane, Y. J. Pendleton, S. B. Porter, F. Scipioni, J. R. Spencer, S. A. Stern, A. J. Verbiscer, H. A. Weaver, R. P. Binzel, M. W. Buie, B. J. Buratti, A. Cheng, A. M. Earle, H. A. Elliott, L. Gabasova, G. R. Gladstone, M. E. Hill, M. Horanyi, D. E. Jennings, A. W. Lunsford, D. J. McComas, W. B. McKinnon, R. L. McNutt, Jr., J. M. Moore, J. W. Parker, E. Quirico, D. C. Reuter, P. M. Schenk, B. Schmitt, M. R. Showalter, K. N. Singer, G. E. Weigle, II and A. M. Zangari, *Science*, 2020, **367**(6481), eaay3705, DOI: 10.1126/science.aay3705.

22 M. Sewilo, S. B. Charnley, P. Schilke, V. Taquet, J. M. Oliveira, T. Shimonishi, E. Wirstrom, R. Indebetouw, J. L. Ward, J. T. van Loon, J. Wiseman, S. Zahorecz, T. Onishi, A. Kawamura, C.-H. R. Chen, Y. Fukui and R. H. Golshan, *ACS Earth Space Chem.*, 2019, **3**, 2088–2109.

23 B. Mueller, B. M. Giuliano, M. Goto and P. Caselli, *Astron. Astrophys.*, 2021, **652**, A126.

24 A. C. A. Boogert, P. A. Gerakines and D. C. B. Whittet, *Annu. Rev. Astron. Astrophys.*, 2015, **53**, 541–581, DOI: 10.1146/annurev-astro-082214-122348.

25 G. W. Fuchs, H. M. Cuppen, S. Ioppolo, C. Romanzin, S. E. Bisschop, S. Andersson, E. F. van Dishoeck and H. Linnartz, *Astron. Astrophys.*, 2009, **505**, 629–639.

26 I. Jimenez-Serra, A. I. Vasyunin, P. Caselli, N. Marcelino, N. Billot, S. Viti, L. Testi, C. Vastel, B. Lefloch and R. Bachiller, *Astrophys. J. Lett.*, 2016, **830**, L6.

27 D. Skouteris, N. Balucani, C. Ceccarelli, N. F. Lago, C. Codella, S. Falcinelli and M. Rosi, *Mon. Not. R. Astron. Soc.*, 2019, **482**, 3567–3575.

28 A. J. Ocana, S. Blazquez, A. Potapov, B. Ballesteros, A. Canosa, M. Antinolo, L. Vereecken, J. Albaladejo and E. Jimenez, *Phys. Chem. Chem. Phys.*, 2019, **21**, 6942–6957.

29 H. Lee, M. Drucker and N. Adams, *Int. J. Mass Spectrom. Ion Processes*, 1992, **117**, 101–114.

30 V. Anicich, An Index of the Literature for Bimolecular Gas Phase Cation-Molecule Reaction Kinetics, 2003, Available at: http://hdl.handle.net/2014/7981.

31 J. Moryl and J. Farrar, *J. Phys. Chem.*, 1982, **86**, 2020–2027.

32 T. Schindler, C. Berg, G. Niedner-Schatteburg, V. Bondybey, C. Lugez, A. Schriver and L. Schriver, *J. Phys. Chem.*, 1994, **98**, 4316–4319.

33 V. Wakelam, J.-C. Loison, E. Herbst, B. Pavone, A. Bergeat, K. Béroff, M. Chabot, A. Faure, D. Galli, W. D. Geppert, D. Gerlich, P. Gratier, N. Harada, K. M. Hickson, P. Honvault, S. J. Klippenstein, S. D. L. Picard, G. Nyman, M. Ruaud, S. Schlemmer, I. R. Sims, D. Talbi, J. Tennyson and R. Wester, *Astrophys. J., Suppl. Ser.*, 2015, **217**, 20.

34 D. McElroy, C. Walsh, A. J. Markwick, M. A. Cordiner, K. Smith and T. J. Millar, *Astron. Astrophys.*, 2013, **550**, A36.

35 D. Ascenzi, A. Cernuto, N. Balucani, P. Tosi, C. Ceccarelli, L. M. Martini and F. Pirani, *Astron. Astrophys.*, 2019, **625**, A72.

36 A. Cernuto, F. Pirani, L. M. Martini, P. Tosi and D. Ascenzi, *ChemPhysChem*, 2018, **19**, 51–59.

37 A. Cernuto, P. Tosi, L. M. Martini, F. Pirani and D. Ascenzi, *Phys. Chem. Chem. Phys.*, 2017, **19**, 19554–19565.

38 B. Friedrich, D. Pullman and D. Herschbach, *J. Phys. Chem.*, 1991, **95**, 8118–8129.

39 B. Friedrich and D. Herschbach, *Nature*, 1991, **353**, 412–414.

40 D. Ascenzi, N. Cont, G. Guella, P. Franceschi and P. Tosi, *J. Phys. Chem. A*, 2007, **111**, 12513–12523.

41 P. Franceschi, L. Penasa, D. Ascenzi, D. Bassi, M. Scotoni and P. Tosi, *Int. J. Mass Spectrom.*, 2007, **265**, 224–229.
42 E. R. Fisher and P. Armentrout, *J. Phys. Chem.*, 1991, **95**, 4765–4772.
43 E. Teloy and D. Gerlich, *Chem. Phys.*, 1974, **4**, 417–427.
44 K. M. Douglas and S. D. Price, *J. Chem. Phys.*, 2009, **131**, 224305.
45 G. Burton, W. Chan, G. Cooper and C. Brion, *Chem. Phys.*, 1992, **167**, 349–367.
46 S. Tanner, G. Mackay and D. Bohme, *Can. J. Chem.*, 1979, **57**, 2350–2354.
47 T. Dang and V. Bierbaum, *Int. J. Mass Spectrom. Ion Proc.*, 1992, **117**, 65–82.
48 A. Kramida, Y. Ralchenko and J. Reader, *NIST Atomic Spectra Database (version 5.8), [Online]*, 2020.
49 B. Ruscic and D. Bross, *Active Thermochemical Tables (ATcT) values based on ver. 1.122p of the Thermochemical Network, [Online]*, 2020.
50 W. Wagner-Redeker, P. Kemper, M. Jarrod and M. Bowers, *J. Chem. Phys.*, 1985, **83**, 1121–1131.
51 J. Herbon, R. Hanson, D. Golden and C. Bowman, *Proc. Combust. Inst.*, 2002, **29**, 1201–1208.
52 D. E. Woon and E. Herbst, *Astrophys. J., Suppl. Ser.*, 2009, **185**, 273.
53 S. Prasad and W. Huntress, *Astrophys. J., Suppl. Ser.*, 1980, **43**, 1–35.
54 K. Goswami, A. Arora, A. Bharadvaja and K. Baluja, *Eur. Phys. J. D*, 2021, **75**, 228.
55 K. L. Nixon, W. A. D. Pires, R. F. C. Neves, H. V. Duque, D. B. Jones, M. J. Brunger and M. C. A. Lopes, *Int. J. Mass Spectrom.*, 2016, **404**, 48–59, DOI: 10.1016/j.ijms.2016.05.006.
56 A. Zavilopulo, F. Chipev and L. Kokhtych, *Nucl. Instrum. Methods Phys. Res., Sect. A*, 2005, **233**, 302–306.
57 S. Srivastava, E. Krishnakumar, A. F. Fucaloro and T. van Note, *J. Geophys. Res.*, 1996, **101**, 26155–26160.
58 K. Refaey and W. Chupka, *J. Chem. Phys.*, 1968, **48**, 5205–5219.
59 J. Berkowitz, *J. Chem. Phys.*, 1978, **69**, 3044–3054.
60 T. Nishimura, Y. Niwa, T. Tsuchiya and H. Nozoye, *J. Chem. Phys.*, 1980, **72**, 2222–2225.
61 S. Borkar, B. Sztaray and A. Bodi, *Phys. Chem. Chem. Phys.*, 2011, **13**, 13009–13020.
62 D. Catone, M. Satta, M. C. Castrovilli, P. Bolognesi, L. Avaldi and A. Cartoni, *Chem. Phys. Lett.*, 2021, **771**, 138467.
63 C. Lavin, M. V. Vega and A. M. Velasco, *J. Phys. Chem. A*, 2012, **116**, 11913–11919.
64 S. Pilling, R. Neves, A. C. F. Santos and H. M. Boechat-Roberty, *Astron. Astrophys.*, 2007, **464**, 393–398.
65 C. Li, C.-H. Chin, T. Zhu and J. Z. H. Zhang, *J. Mol. Struct.*, 2020, **1217**, 128410.
66 NIST Computational Chemistry Comparison and Benchmark Database, NIST Standard Reference Database Number 101, ed. R. D. Johnson III, https://cccbdb.nist.gov/, Release 21, August 2020.
67 M. Gussoni, R. Rui and G. Zerbi, *J. Mol. Struct.*, 1998, **447**, 163–215.
68 A. D. Becke, *J. Chem. Phys.*, 1993, **98**, 1372–1377.
69 P. J. Stephens, F. J. Devlin, C. F. Chabalowski and M. J. Frisch, *J. Phys. Chem.*, 1994, **98**, 11623–11627.
70 T. H. Dunning Jr, *J. Chem. Phys.*, 1989, **90**, 1007–1023.
71 D. E. Woon and T. H. Dunning Jr, *J. Chem. Phys.*, 1993, **98**, 1358–1371.
72 F. Pirani, S. Brizi, L. F. Roncaratti, P. Casavecchia, D. Cappelletti and F. Vecchiocattivi, *Phys. Chem. Chem. Phys.*, 2008, **10**, 5489–5503.
73 F. Pirani, G. Maciel, D. Cappelletti and V. Aquilanti, *Int. Rev. Phys. Chem.*, 2006, **25**, 169.
74 P. Linstorm, *J. Phys. Chem. Ref. Data, Monogr.*, 1998, **9**, 1–1951.
75 M. B. Robin and N. A. Kuebler, *J. Electron Spectrosc. Relat. Phenom.*, 1972/73, **1**, 13–28.
76 S. Thurmer, T. Shinno and T. Suzuki, *J. Phys. Chem. A*, 2021, **125**, 2492–2503.
77 R. Candori, S. Cavalli, F. Pirani, A. Volpi, D. Cappelletti, P. Tosi and D. Bassi, *J. Chem. Phys.*, 2001, **115**, 8888–8898.
78 R. Candori, F. Pirani, D. Cappelletti, P. Tosi and D. Bassi, *Int. J. Mass Spectrom.*, 2003, **223**, 499–506.
79 C. Zener, *Proc. R. Soc. London, Ser. A*, 1932, **137**, 696–702.
80 E. Nikitin and S. Umanskii, *Theory of Slow Atomic Collisions*, aus: Springer Series in Chemical Physics, 1984, vol. 30.
81 E. Nikitin, *Annu. Rev. Phys. Chem.*, 1999, **50**, 1–21.
82 M. Rosi, L. Mancini, D. Skouteris, C. Ceccarelli, N. F. Lago, L. Podio, C. Codella, B. Lefloch and N. Balucani, *Chem. Phys. Lett.*, 2018, **695**, 87–93.
83 N. Balucani, D. Skouteris, C. Ceccarelli, C. Codella, S. Falcinelli and M. Rosi, *Mol. Astrophys.*, 2018, **13**, 30–37.
84 C. Berteloite, S. D. Le Picard, I. R. Sims, M. Rosi, F. Leonori, R. Petrucci, N. Balucani, X. Wang and P. Casavecchia, *Phys. Chem. Chem. Phys.*, 2011, **13**, 8485–8501.
85 J.-D. Chai and M. Head-Gordon, *Phys. Chem. Chem. Phys.*, 2008, **10**, 6615–6620.
86 R. J. Bartlett, *Annu. Rev. Phys. Chem.*, 1981, **32**, 359–401.
87 K. Raghavachari, G. W. Trucks, J. A. Pople and M. Head-Gordon, *Chem. Phys. Lett.*, 1989, **157**, 479–483.
88 J. Olsen, P. Jørgensen, H. Koch, A. Balkova and R. J. Bartlett, *J. Chem. Phys.*, 1996, **104**, 8007–8015.
89 M. Frisch, G. Trucks, H. Schlegel, G. Scuseria, M. Robb, J. Cheeseman, G. Scalmani, V. Barone, B. Mennucci and G. Petersson, *et al.*, *Gaussian 09, rev. A. 02*, Gaussian, 2009.
90 M. D. Hanwell, D. E. Curtis, D. C. Lonie, T. Vandermeersch, E. Zurek and G. R. Hutchison, *J. Cheminf.*, 2012, **4**, 1–17.
91 C. Li, C.-H. Chin, T. Zhu and J. Z. H. Zhang, *J. Mol. Struct.*, 2020, **1217**, 128410.
92 H. Wu, Y. Xue, J. Wen, H. Wang, Q. Fan, G. Chen, J. Zhu, F. Qu and J. Guo, *RSC Adv.*, 2019, **9**, 16683–16689.
93 N. L. Ma, B. J. Smith, J. A. Pople and L. Radom, *J. Am. Chem. Soc.*, 1991, **113**, 7903–7912.
94 A. Tsikritea, J. A. Diprose, T. P. Softley and B. R. Heazlewood, *Phys. Chem. Chem. Phys.*, 2022, **157**, 060901.

95 *Tutorials in Molecular Reaction Dynamics*, ed. M. Brouard and C. Vallance, RCS Publishing, Cambridge UK, 2010.

96 W. J. Chesnavich, T. Su and M. T. Bowers, *J. Chem. Phys.*, 1980, **72**, 2641–2655.

97 T. Su and W. J. Chesnavich, *J. Chem. Phys.*, 1982, **76**, 5183–5185.

98 Y. Georgievskii and S. J. Klippenstein, *J. Chem. Phys.*, 2005, **122**, 194103.

99 A. Kilaj, J. Wang, P. Stranak, M. Schwilk, U. Rivero, L. Xu, O. A. von Lilienfeld, J. Kupper and S. Willitsch, *Nat. Commun.*, 2021, **12**, 6047.

100 A. D. Doerfler, P. Eberle, D. Koner, M. Tomza, M. Meuwly and S. Willitsch, *Nat. Commun.*, 2019, **10**, 5429.

101 A. Kilaj, H. Gao, D. Rosch, U. Rivero, J. Kuepper and S. Willitsch, *Nat. Commun.*, 2018, **9**, 2096.

102 V. Zhelyazkova, F. B. Martins, V. M. Zesko and F. Merkt, *Phys. Chem. Chem. Phys.*, 2022, **24**, 2843–2858.

103 V. Zhelyazkova, F. B. Martins, V. J. A. Agner, H. Schmutz and F. Merkt, *Phys. Chem. Chem. Phys.*, 2021, **23**, 21606–21622.

104 V. Zhelyazkova, F. B. Martins, V. J. A. Agner, H. Schmutz and F. Merkt, *Phys. Rev. Lett.*, 2020, **125**, 263401.

105 K. Hoveler, J. Deiglmayr and F. Merkt, *Mol. Phys.*, 2021, **119**, 17–18, SI.